Original Article

First-in-human technique translation of oxygen-enhanced MRI to an MR Linac system in patients with head and neck cancer

Michael J. Dubec [a,b,*], David L. Buckley [b,c], Michael Berks [a], Abigael Clough [d], John Gaffney [e], Anubhav Datta [a,f], Damien J. McHugh [a,b], Nuria Porta [g], Ross A. Little [a], Susan Cheung [a], Christina Hague [e], Cynthia L. Eccles [a,d], Peter J. Hoskin [a,h], Robert G. Bristow [a,e], Julian C. Matthews [i], Marcel van Herk [a], Ananya Choudhury [a,e], Geoff J.M. Parker [j,k], Andrew McPartlin [e,l], James P.B. O'Connor [a,f,m]

[a] Division of Cancer Sciences, University of Manchester; [b] Christie Medical Physics and Engineering, The Christie NHS Foundation Trust, Manchester; [c] Biomedical Imaging, University of Leeds, Leeds; [d] Radiotherapy, The Christie NHS Foundation Trust; [e] Clinical Oncology, The Christie NHS Foundation Trust; [f] Radiology, The Christie NHS Foundation Trust, Manchester; [g] Clinical Trials and Statistics Unit, The Institute of Cancer Research, London; [h] Department of Clinical Oncology, Mount Vernon Cancer Centre, Northwood; [i] Neuroscience and Experimental Psychology, University of Manchester; [j] Bioxydyn Ltd, Manchester, UK; [k] Centre for Medical Image Computing, Department of Medical Physics and Biomedical Engineering, University College London, London, UK; [l] Radiation Oncology, Princess Margaret Cancer Center, Toronto, Canada; [m] Division of Radiotherapy and Imaging, The Institute of Cancer Research, London, UK

ARTICLE INFO

ABSTRACT

Background and purpose: Tumour hypoxia is prognostic in head and neck cancer (HNC), associated with poor loco-regional control, poor survival and treatment resistance. The advent of hybrid MRI – radiotherapy linear accelerator or 'MR Linac' systems – could permit imaging for treatment adaptation based on hypoxic status. We sought to develop oxygen-enhanced MRI (OE-MRI) in HNC and translate the technique onto an MR Linac system.

Materials and methods: MRI sequences were developed in phantoms and 15 healthy participants. Next, 14 HNC patients (with 21 primary or local nodal tumours) were evaluated. Baseline tissue longitudinal relaxation time (T_1) was measured alongside the change in $1/T_1$ (termed ΔR_1) between air and oxygen gas breathing phases. We compared results from 1.5 T diagnostic MR and MR Linac systems.

Results: Baseline T_1 had excellent repeatability in phantoms, healthy participants and patients on both systems. Cohort nasal concha oxygen-induced ΔR_1 significantly increased (p < 0.0001) in healthy participants demonstrating OE-MRI feasibility. ΔR_1 repeatability coefficients (RC) were 0.023–0.040 s^{-1} across both MR systems. The tumour ΔR_1 RC was 0.013 s^{-1} and the within-subject coefficient of variation (wCV) was 25% on the diagnostic MR. Tumour ΔR_1 RC was 0.020 s^{-1} and wCV was 33% on the MR Linac. ΔR_1 magnitude and time-course trends were similar on both systems.

Conclusion: We demonstrate first-in-human translation of volumetric, dynamic OE-MRI onto an MR Linac system, yielding repeatable hypoxia biomarkers. Data were equivalent on the diagnostic MR and MR Linac systems. OE-MRI has potential to guide future clinical trials of biology guided adaptive radiotherapy.

Tumours contain hypoxic regions, resulting from an imbalance between oxygen supply and consumption [1]. Hypoxia is prognostic in head and neck cancer (HNC), being associated with both poor loco-regional control and reduced survival [2–3]. In addition, hypoxia impedes radiation treatment by hindering production of free radicals for tumour DNA damage. Consequently, greater radiation dose is required to cause the same tumour damage compared to normoxic microenvironments [4–5]. There is strong evidence that combining hypoxia-modification with radiotherapy improves loco-regional control [6] and overall survival in patients with HNC [7]. Furthermore, hypoxia limits the effectiveness of chemotherapy and immunotherapy [8].

Identifying, mapping and quantifying tumour hypoxia before treatment and following re-oxygenation during radiotherapy may improve stratification of patients based on their hypoxic status. This may assist biology guided adaptive radiotherapy [3,9–10]. Invasive oxygen electrode measurements, gene signatures [11], immunohistochemistry (IHC) based biomarkers [12] and endogenous blood-based biomarkers [13] can identify hypoxia but do not provide spatial information, track temporal change, or enable

analysis of multiple lesions with distinct biology without serial invasive sampling. These factors are all important when considering personalised radiotherapy [5].

PET imaging can non-invasively measure tumour hypoxia and monitor hypoxic changes through treatment. However, PET requires specialist radiochemistry, expensive radiopharmaceuticals and local expertise, which has hindered widespread clinical adoption [14]. Oxygen-enhanced magnetic resonance imaging (OE-MRI) offers a practical and readily translatable technique to assess oxygenation in normal tissues and tumours with spatial resolution superior to PET [15]. In OE-MRI, change in longitudinal relaxation rate (R_1) of blood and tissues is measured following inhalation of 100% oxygen or carbogen [16]. Inhaled oxygen molecules dissolve in the blood plasma and interstitial fluid, inducing an increase in R_1 (ΔR_1) via a paramagnetic contrast effect [17]. Studies on preclinical and clinical diagnostic MR systems show that OE-MRI can identify, quantify and map hypoxia in animal and human tumour types and track changes induced by radiotherapy [17–19]. R_1 based OE-MRI is distinct from Blood Oxygen Level Dependent (BOLD) imaging which measures changes in the haemoglobin associated effective transverse relaxation rate (R_2^*) [20] and is susceptible to magnetic field inhomogeneities from air-tissue interfaces found in head and neck anatomy.

OE-MRI is an attractive technique to monitor tumour oxygenation on hybrid systems that combine real-time MRI with radiotherapy delivery. These systems facilitate personalised biology guided adaptive radiotherapy by targeting hypoxic tissue through dose painting or other techniques [9]. However, there are several expected challenges in translating such techniques from diagnostic systems to an MR Linac system. These include hardware differences associated with receive coil and gradient systems [21], the requirement for ancillary equipment within the radiotherapy bunker [22–23] and demonstration that OE-MRI biomarkers derived on the MR Linac are comparable to those derived on diagnostic systems. The aims of this work were to demonstrate OE-MRI feasibility and repeatability on an MR Linac system in healthy participants and in HNC patients.

Materials and methods

Scanner hardware

OE-MRI was established and implemented on two systems; a 1.5 T MR scanner used in standard diagnostic healthcare (Philips Ingenia MR-RT system, Philips Medical Systems, Philips MR software version 5.7.1), herein referred to as 'diagnostic MR system' and a 1.5 T MR Linac system (Elekta Unity, Philips MR software version 5.7.1).

On the diagnostic MR system, a 16-channel posterior spinal array, a 32-channel large flexible anterior array, positioned on a coil bridge, and two single channel loop coils positioned laterally, were used. On the MR Linac system, a 4-channel posterior array and a 4-channel anterior array, positioned on a coil bridge, were used. Imaging on both systems was performed on a flat table-top to mimic radiotherapy setup.

Imaging protocol and equipment

Imaging sequences were optimised in phantoms and healthy participants on the diagnostic MR system. Finalised sequences were replicated as close as possible on the MR Linac system. A schematic of the imaging protocols (Supplementary Fig. 1) and sequence parameters (Supplementary Table 1) are provided.

All imaging was acquired in the transverse plane without slice gaps. Healthy participants and patients all initially breathed medical air during acquisition of a T_2w fast-spin echo (FSE)

anatomical image and a baseline 3D inversion recovery turbo field echo (IRTFE) T_1 map with five inversion pre-pulse delays. This was followed by the 3D dynamic IRTFE sequence (OE-MRI acquisition with 12 s temporal resolution, consisting of initial scans 1–25 of the IRTFE dynamic sequence; scan time 5 minutes). Then, gas delivery was switched to 100% O_2 for scans 26–70 of the dynamic sequence (9 minutes), before returning to medical air breathing on scans 71–91 (4 minutes). Following this, a 3D fat-saturated T_1w FFE was acquired. In HNC patients only, contrast agent (gadoterate meglumine (Dotarem, Guerbet), 0.2 mol/kg at 3 ml/s, 20 ml flush) was delivered to facilitate tumour contouring on the T_1w FFE sequence. Contrast agent was delivered by contrast power injector (MRExperion, Bayer) installed on both systems.

Modifications were required to the MR Linac system room to install medical air and oxygen from the magnet room supply ports to a low-flow air-oxygen gas blender (Inspiration Healthcare) to deliver either 21% or 100% O_2. Gases passed through a flowmeter to control flow at continuous 15 l/min and then through flexible tubing to a non-rebreathe oxygen mask (Ecolite™, Intersurgical Ltd). This circuit ensured similar gas delivery to our diagnostic systems [18], where waveguides allow gas hoses and tubing to be passed between the control room and the magnet room (Supplementary Fig. 2).

Phantom data acquisition

Sequence evaluation was performed using a Eurospin TO5 phantom (Eurospin, Diagnostic Sonar). Prior to imaging, the phantom was left in the diagnostic MR system room for temperature stabilisation at the ambient room temperature of 24 °C. The phantom was immediately transferred to the MR Linac following diagnostic MR system measurements to minimise temperature changes in the gel samples between imaging on the different systems. The phantom imaging protocol (Supplementary Fig. 1) consisted of repeated baseline T_1 measurements, carried out 20 minutes apart. In addition, the presence of drift in the dynamic IRTFE measurement was evaluated in the absence of the gas challenge.

Data acquisition in healthy participants and patients

All participants were recruited after research ethics approval and provided written informed consent (ClinicalTrials.gov identifiers: NCT04903236 and NCT03646747).

Initial protocol development was in 4 healthy participants (data not included). The resultant locked protocol was acquired in 6 healthy participants using the diagnostic MR and equivalent protocol was acquired in 5 different healthy participants using the MR Linac system.

The locked protocols were then tested for feasibility in 3 patients on the diagnostic MR system. Then data were acquired in 6 HNC patients using the diagnostic MR system and 5 different HNC patients using the MR Linac system.

Data processing and image analysis

In phantoms, baseline T_1 maps were calculated using a region of interest (ROI) positioned in the central slice of each gel sample. Linear fitting was performed on the dynamic IRTFE data to assess drift. In human subjects, motion correction of dynamic OE-MRI data and registration of pre-gas-challenge (baseline) T_1 mapping and dynamic OE-MRI datasets was carried out for all participants using a deformable registration method in Elastix [24].

Baseline T_1 maps were derived by non-linear least squares fitting to the signal data (S(TI)) acquired at five inversion pre-pulse delay times (TI). The IRTFE sequence employed a repetition time (TR) > 5 T_1 and very short echo time (TE), such that the TR and TE terms can be ignored. For this reason, the non-linear fit estimation of T_1 reads as:

$$S(TI) = S_0 \left| 1 - 2\lambda \exp\left(\frac{-TI}{T_1}\right) \right| \tag{1}$$

Here, S_0 is the equilibrium signal, TI is the previously described inversion pre-pulse delay time and λ is the inversion efficiency parameter. S_0, T_1 and λ were fit as free parameters. Measurement of baseline T_1 then permitted the conversion of dynamic signal change ($\Delta SI(t)$) to $\Delta R_1(t)$ (where, $\Delta R_1(t) = R_{1,O2} - R_{1,air}$) [25]. $R_{1,air}$ was calculated as the median of ΔR_1 measurements 2–25 acquired during the air phase and $R_{1,O2}$ values was calculated as the median of dynamic measurements 60–70 acquired during the 100% oxygen phase.

In healthy participants, ΔR_1 measurements were obtained from a ROI positioned within the nasal concha and the tongue. In patients, primary tumours and any local metastatic lymph nodes were outlined on T_1w FFE gadolinium enhanced contrast images by a clinical oncologist (6 years' experience) and transferred to the motion corrected datasets allowing lesion ΔR_1 estimation. Contouring was carried out using JIM software (JIM 6, Xinapse Systems).

Whole ROI analysis measured ΔR_1 in the nasal concha and tongue of healthy participants and in tumour lesions in patients. In addition, ΔR_1 maps were produced from voxel-wise processing to provide spatial representation of the oxygen-induced ΔR_1 changes within the lesion.

Statistical analysis

Phantom T_1 data was assessed by Bland Altman analysis and limits of agreement (LOA) (cohort mean (μ) ± 1.96 standard deviation (σ)) are presented [26]. We compared μ and σ of healthy participants and HNC patient T_1 and ΔR_1 estimates and derived the repeatability coefficient (RC) and within-subject coefficient of variation (wCV) from repeat measurements [27]. In this small cohort, repeat measurements were deemed to show no significant difference if there was overlap in their corresponding 95% confidence intervals on RC [27–29]. Oxygen-induced change in ΔR_1 was assessed by unpaired t-test between ΔR_1 measurements on air vs oxygen breathing, $p < 0.05$ was deemed significant in this work. Data processing and analysis was carried out using MATLAB (Mathworks).

Results

Phantom T_1 measurements were derived (Supplementary Fig. 3) and their repeatability was determined for each MR system and across systems (Supplementary Fig. 4). On the diagnostic MR, the difference in mean T_1 was (μ ± σ) −4.0 ± 6.2 ms (LOA = -16.2 to 8.1 ms). In comparison, on the MR Linac, the difference in mean T_1 was −6.9 ± 6.6 ms (LOA = -20.0 to 6.1 ms). Agreement between the two MRI systems was assessed (Supplementary Fig. 4) and the difference in mean T_1 was 2.3 ± 22 ms (LOA = -40.0 to 44.5 ms).

Signal drift during the dynamic sequence used for OE-MRI measurements was assessed on both MRI systems. The signal courses for each of four representative T_1 gel tubes were linear, horizontal, and showed no upward or downward trends during the 18 minute acquisition on either system (Supplementary Fig. 5). Linear fitting to the dynamic IRTFE data in these gels showed the largest ΔR_1

drift measured were $\Delta R_1 = 1.4\times10^{-5}$ min^{-1} s^{-1} and $\Delta R_1 = 6.0\times10^{-5}$ min^{-1} s^{-1} on the diagnostic MR and MR Linac systems respectively. Collectively, this shows that phantom T_1 measurements are repeatable and free of drift on both the diagnostic MR and the MR Linac.

Next, we evaluated if OE-MRI could be tolerated on the MR Linac and detect oxygen inhalation in normal tissues. Following sequence optimisation and protocol standardisation, in 4 healthy participants, locked down protocols were performed in a further 11 healthy participants (6 on diagnostic MR and 5 on MR Linac). No adverse events were reported. Hyperoxic gas breathing was well tolerated in all participants. Each participant had two scan visits (B1 and B2) evaluating the nasal concha and the tongue, at 13.4 ± 21.7 days apart. All datasets were deemed suitable for inclusion in analysis, following motion correction and registration.

On the diagnostic MR, the mean cohort baseline T_1 (±σ) of the nasal concha was 1214 (±28) ms for B1 and 1208 (±51) ms for B2 (RC of 107 ms (95% CI: 69–235 ms) and wCV of 3%). By comparison, on the MR Linac the mean cohort baseline T_1 (±σ) of the nasal concha was 1206 (±41) ms for B1 and 1218 (±41) ms for B2 (RC of 79 ms (95% CI: 49–192 ms) and wCV of 2%; Fig. 1, A-B).

The cohort ΔR_1 induced by oxygen challenge was significant in the nasal concha on both MR systems ($p < 0.0001$) and ΔR_1 time-course curves appeared similar in shape and magnitude on both MR systems (Fig. 1, C-D). This indicated that OE-MRI could detect oxygen inhalation on both systems. On the diagnostic MR system ΔR_1 in the nasal concha was 0.052 (±0.020) s^{-1} for B1 and 0.062 (±0.029) s^{-1} for B2 (RC of 0.040 s^{-1} (95% CI: 0.026–0.089 s^{-1}) and wCV of 25%). By comparison, on the MR Linac the ΔR_1 in the nasal concha was 0.061 (±0.009) s^{-1} for B1 and 0.055 (±0.013) s^{-1} for B2 (RC of 0.023 s^{-1} (95% CI: 0.015–0.057 s^{-1}) and wCV of 15%; Fig. 1, E-F).

The cohort ΔR_1 induced by oxygen challenge was also significant in the tongue measured on the diagnostic MR ($p = 0.03$) and MR Linac systems ($p = 0.0003$). However, the magnitude of change was substantially less than that seen in the nasal concha (Supplementary Table 2 and Supplementary Fig. 6).

We then evaluated feasibility in 3 patients on the diagnostic MR system. Clinical details are provided in Supplementary Table 3. In each patient, a statistically significant oxygen ΔR_1 was detected, resulting in oxygen-induced changes of 0.018, 0.032 and 0.010 s^{-1} respectively ($p < 0.0001$) (Fig. 2). This shows that OE-MRI can be performed with dynamic, volumetric IR-based sequences that cover the head and neck region in a clinically practicable timescale.

Next, we evaluated repeatability of OE-MRI in a further 11 patients scanned twice (B1 and B2) using the locked protocol at 5.6 ± 1.6 days apart. Details of patient age, gender, tumour histology, stage and target lesions imaged are listed in Table 1. Again, no adverse events were reported and hyperoxic gas breathing was well tolerated in all patients. Analysis proceeded in 6 diagnostic MR system patients (5 primary tumours; 6 nodal metastases) and 5 MR Linac system patients (5 primary tumours; 2 nodal metastases), resulting in 18 lesions available for evaluation. Sample ΔR_1 maps are shown in Fig. 3 and show spatial similarity between B1 and B2. All datasets except one (see Table 1; patient 5, tumour) were deemed suitable for inclusion in analysis, following motion correction and registration.

Median values and repeatability of lesion baseline T_1 and oxygen-induced ΔR_1 are summarised in Table 2 and Fig. 4. OE-MRI ΔR_1 time-course curves appeared equivalent in shape and magnitude across both MR systems. The cohort ΔR_1 induced by oxygen challenge was significant for patient lesions on both MR systems ($p < 0.0001$). This shows that OE-MRI is repeatable and detects tumour hypoxia.
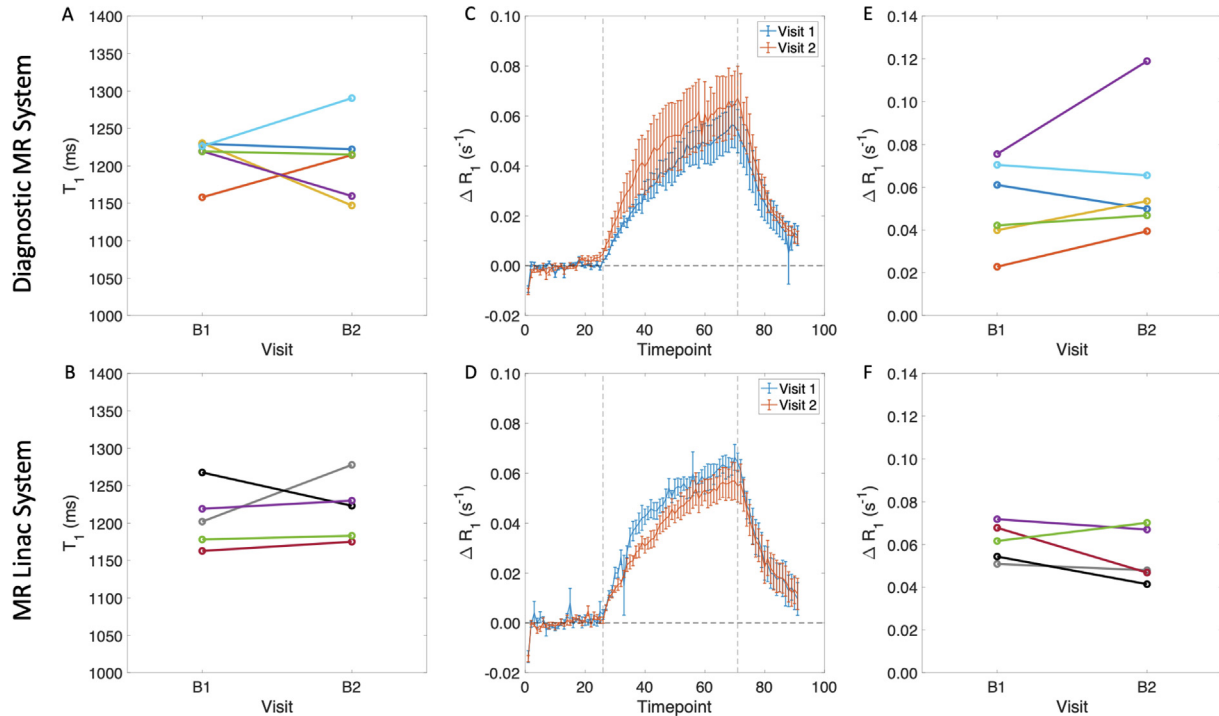
Fig. 1. OE-MRI derived signal changes in the nasal concha are feasible and repeatable in healthy participants: Baseline T_1 measurements acquired on the (A) diagnostic and (B) MR Linac systems are repeatable. The ΔR_1 ($\mu \pm$ SEM) time-courses obtained from two visits from the (C) diagnostic and (D) MR Linac systems have similar magnitude, duration and shape. The ΔR_1 measured on the (E) diagnostic and (F) MR Linac systems are repeatable. In figures A, B, E and F, each colour represents a participant. Vertical dashed lines on the ΔR_1 time-courses (C and D) indicate the timepoints at which the gas was switched between air to oxygen (timepoint 26) and oxygen to air (timepoint 71).

Discussion

The MR Linac presents an opportunity to map and quantify tumour function daily or several times per week, in addition to tracking change in tumour size and position. Quantitative imaging techniques including diffusion weighted imaging (DWI) [30], intravoxel-incoherent motion (IVIM) [31], T_1 and T_2 relaxometry [32] and chemical exchange saturation transfer (CEST) [33] have been described on MR Linac systems. However, few of these techniques yield biomarkers that measure aspects of the tumour microenvironment with proven clinical relevance. In distinction, imaging hypoxia – a well-recognised prognostic and predictive indicator of outcome following radiotherapy – has clear rapid translational potential.

Prior to this study, we and others have demonstrated that OE-MRI can induce signal changes in healthy tissues [16,34], can identify, quantify and map hypoxic sub-regions in mouse [17–18], rat [19], rabbit [35] and human [36–39] tumours, and can track response to therapy in patients with lung cancer [18]. While our previous work has focused on the value of OE-MRI combined with a perfusion sequence to exclude necrosis [17–18], most of the studies listed above from other groups tend to perform OE-MRI without this additional step. In this work, we have performed a first-in-human translation of OE-MRI as a standalone sequence onto the MR Linac and demonstrated its feasibility and repeatability in HNC patients.

We initially evaluated the OE-MRI protocol using phantoms to confirm T_1 measurement repeatability and assess drift in dynamic measurements. This is important since the baseline T_1 measurement is used to convert the oxygen-induced signal change to ΔR_1, which is effectively proportional to oxygen concentration in tissue [20]. We then installed a permanent supply of oxygen and medical air from the main hospital gas supply through the

MR Linac bunker to the treatment room. New gas panel interface and gas ports were installed without the need for magnet ramp down.

Following optimisation of MR sequences in a cohort of healthy participants on the diagnostic 1.5 T system, we replicated T_1 mapping and dynamic OE-MRI sequences on the MR Linac. We identified the nasal concha as a valuable reference region to confirm oxygen delivery in healthy subjects. Both diagnostic MR and MR Linac protocols were sensitive to oxygen-induced T_1 change in tissues including the nasal concha. Importantly all aspects of signal evaluation – the shape and magnitude of the dynamic curve, the temporal response to gas challenge, the variation between subjects, the repeatability between baseline scan episodes – were equivalent on the MR Linac and our diagnostic system at 1.5 T, despite differences in receive coil and gradient performance – due to the split gradient system of the MR Linac (slight increase of TR by 0.2 ms and TE by 0.1 ms on the MR Linac was deemed acceptable) [21].

We then translated OE-MRI to evaluate patients with HNC on both the diagnostic MR system, to define system performance, and then on the MR Linac. Again, we showed that the shape and magnitude of the dynamic curve, the within subject variation, the repeatability and the temporal response to gas challenge were equivalent across the two systems. Practical constraints prevented data being acquired from the same participants across both the diagnostic MR and the MR Linac, but despite this data appeared very similar across both platforms.

Data quality was formally assessed. One lesion dataset was corrupted by motion beyond recovery using our registration technique, but otherwise we were successful in applying dynamic, volumetric IR-based OE-MRI in 15 healthy participants (26 scans) and in 14 HNC patients (25 scans) with a success rate of 50/51 (i.e. 98%). Further, ΔR_1 repeatability was measured for each MRI
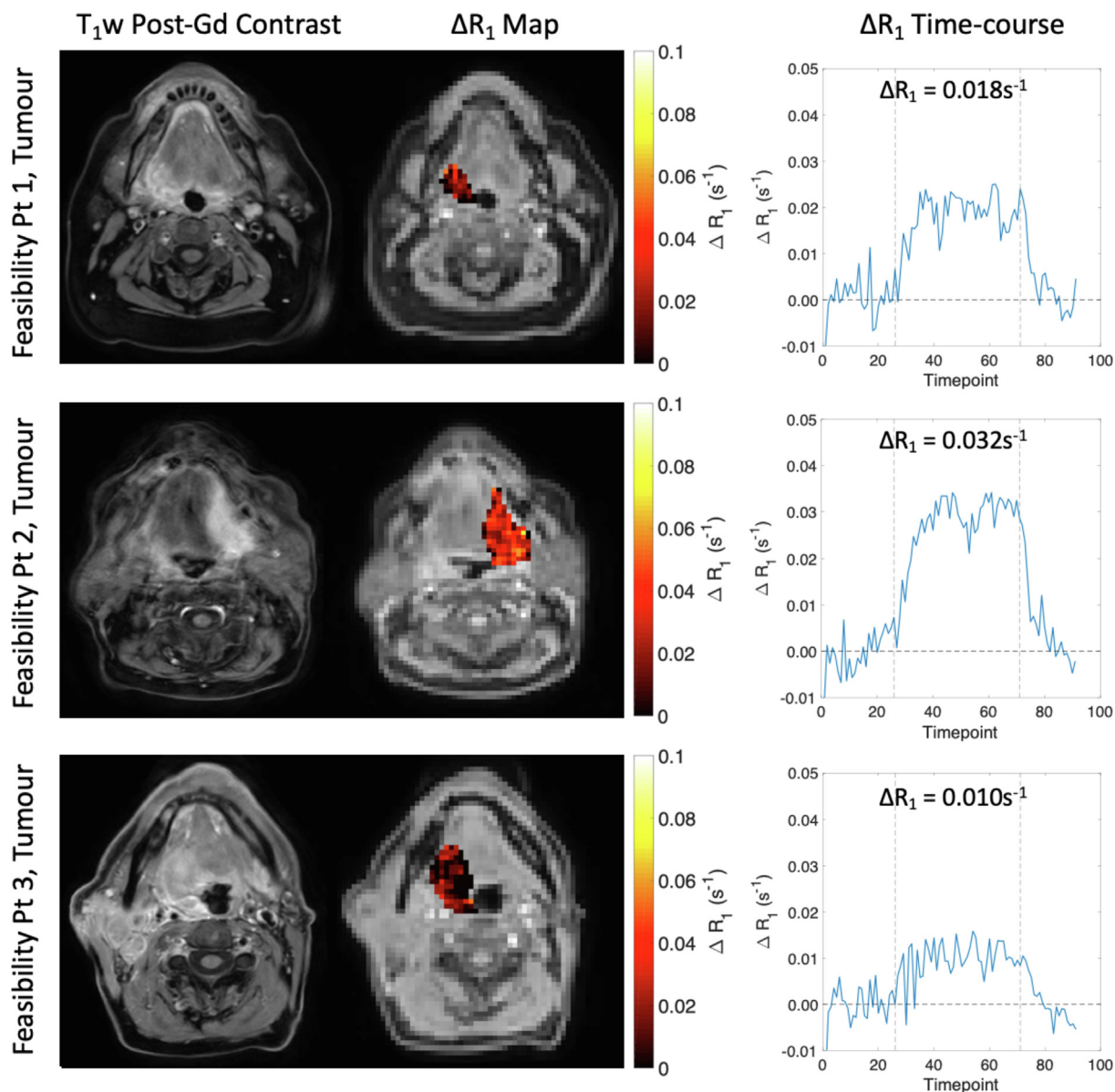
Fig. 2. Data from the three OE-MRI feasibility patients, showing the post-contrast T_1w image for anatomical reference (left column), along with the ΔR_1 map derived from the single visit (middle column) and the mean ΔR_1 time-course obtained from the contoured tumour (right column). Vertical dashed lines on the time-course indicate the timepoints at which the gas was switched between air to oxygen (timepoint 26) and oxygen to air (timepoint 71).

Table 1
Patient information. Lesions; T = primary tumour and N = local metastatic lymph node.

Patient ID	Sex	Age	Disease Site	TNM Stage	Imaging System	Target Lesion(s)
1	F	73	Tonsil	T3N1	Diagnostic MR	T
2	M	72	Tonsil	T2N1	Diagnostic MR	T, N
3	M	64	Tonsil	T3N2b	Diagnostic MR	T, N
4	M	57	Tonsil	T3N2b	Diagnostic MR	T, N, N
5	M	67	Base of tongue	T1N2c	Diagnostic MR	T*, N
6	M	74	Base of tongue	T4N1	Diagnostic MR	T, N
7	M	65	Tonsil	T2N0	MR Linac	T
8	M	65	Base of tongue	T1N3b	MR Linac	T
9	M	60	Tonsil	T3N2b	MR Linac	T, N
10	M	77	Base of tongue	T1N1	MR Linac	T, N
11	F	45	Hypopharynx	T2N0	MR Linac	T

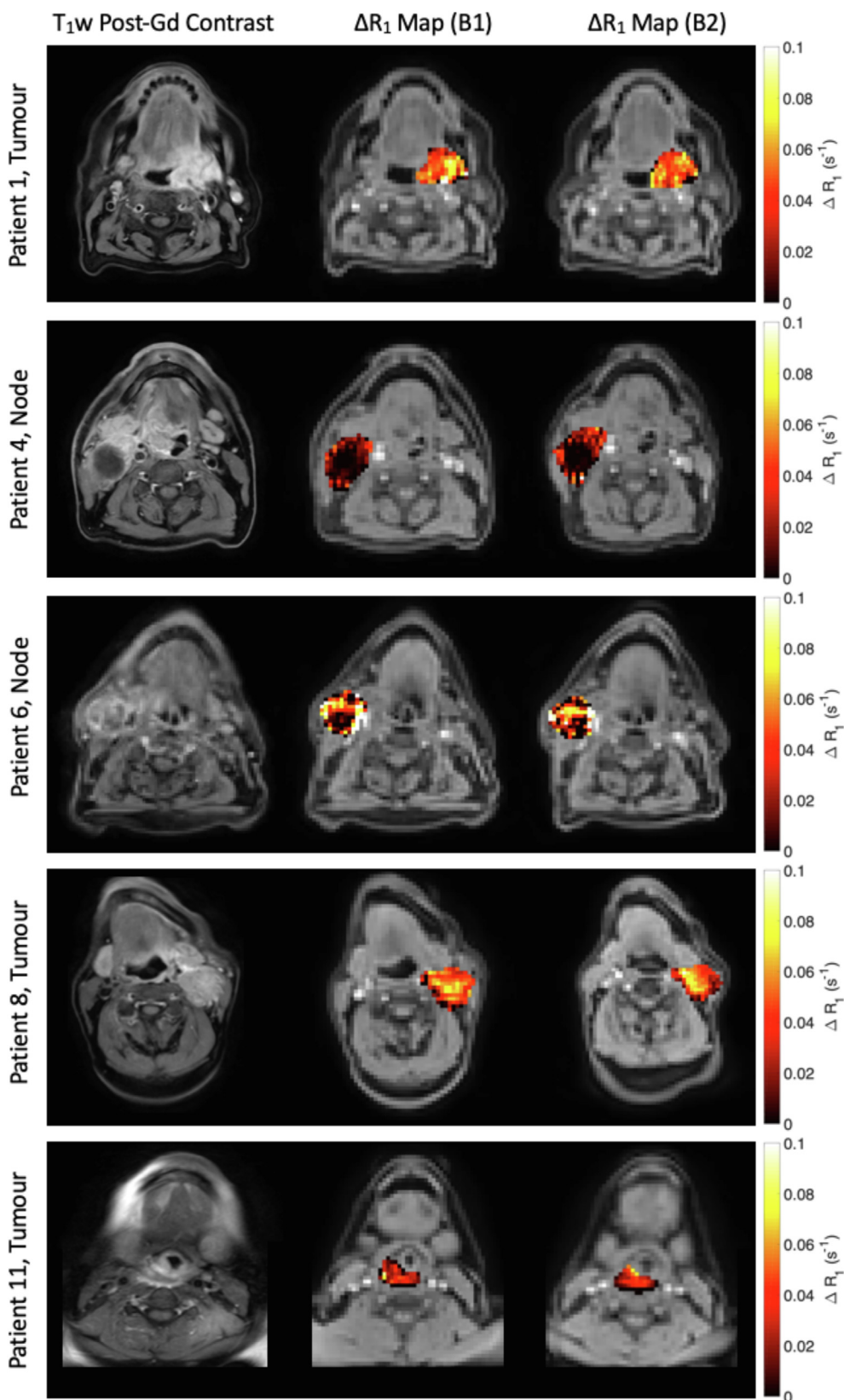*motion corrupted and not used in final analysis.

Fig. 3. Example images obtained from five patients in this study. A post-contrast T_1w image from timepoint B1 (left column) is provided for anatomical reference and ΔR_1 maps obtained from pre-treatment baseline timepoints (middle column) B1 and (right column) B2 are shown for visual comparison of repeatability.

platform for both healthy participants and patients with HNC using RCs. These values (between 0.013 to 0.040 s^{-1}) are a benchmark for future studies and provide a means to evaluate significance of change between OE-MRI scans in future studies

performed with an equivalent scanner on an equivalent patient population. Additionally, our ΔR_1 results are of the same order of magnitude as those described elsewhere in literature at 1.5 T [18,38,40].

Table 2
T_1 and ΔR_1 measurements for patient lesions on the diagnostic and MR Linac systems.

Parameter	System	Patients, Lesions	B1 ($\mu \pm \sigma$)	B2 ($\mu \pm \sigma$)	RC (95%CI)	wCV
T_1 (ms)	**Diagnostic MR**	6 Patients, 11 Lesions (5 T, 6 N)	1144 ± 77	1134 ± 68	78 (56–133)	2%
	MR Linac	5 Patients 7 Lesions (5 T, 2 N)	1153 ± 33	1136 ± 42	59 (33–120)	2%
ΔR_1 (s^{-1})	**Diagnostic MR**	6 Patients 11 Lesions (5 T, 6 N)	0.019 ± 0.013	0.019 ± 0.010	0.013 (0.010–0.023)	25%
	MR Linac	5 Patients 7 Lesions (5 T, 2 N)	0.021 ± 0.010	0.024 ± 0.013	0.020 (0.014–0.042)	33%

B1 = baseline visit 1, B2 = baseline visit 2. T = primary tumour, N = local metastatic lymph node. RC = repeatability coefficient, wCV = within-subject coefficient of variation.
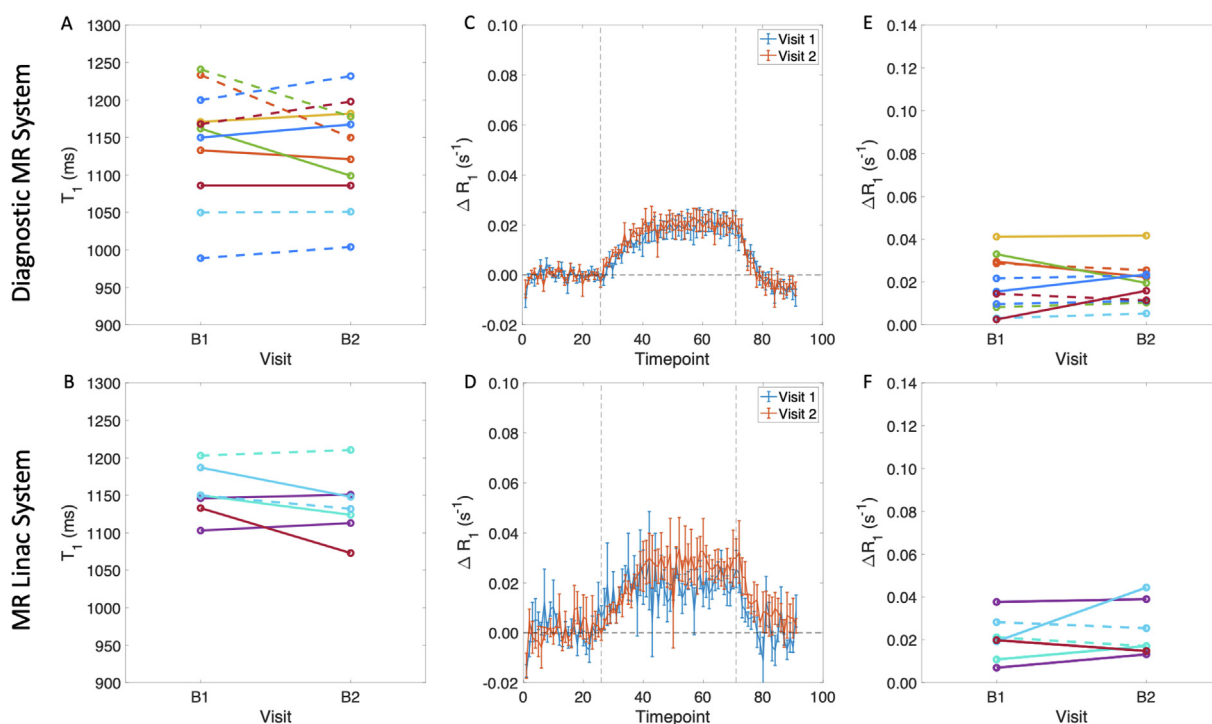

Fig. 4. OE-MRI derived in HNC patient tumours are repeatable. Baseline T_1 measurements acquired on the (A) diagnostic and (B) MR Linac systems are repeatable; ΔR_1 ($\mu \pm$ SEM) time-courses obtained from two visits from the (C) diagnostic and (D) MR Linac systems have similar magnitude, duration and shape. The ΔR_1 measured on the (E) diagnostic and (F) MR Linac systems are repeatable. In figures A, B, E and F, each colour represents a patient, solid lines represent primary tumours and dashed lines represent lymph nodes. Vertical dashed lines on the ΔR_1 time-courses (C and D) indicate the timepoints at which the gas was switched between air to oxygen (timepoint 26) and oxygen to air (timepoint 71).

Limitations of our work include the need to shorten the protocol described here to enable a revised version to fit into the MR Linac workflow – from 40 minutes in this work to 15 minutes or less; the need to add in a perfusion sequence such as DCE-MRI [41] to exclude regions of necrosis; potential need for optimisation using thermoplastic shells for immobilisation, as is commonplace for neck radiotherapy, and the need to establish multisite feasibility and reproducibility across distinct geographical sites [42–43].

In summary, we have successfully performed OE-MRI in patients with HNC. We then performed first-in-human application of OE-MRI on a MR Linac. Further work is underway to assess treatment response and dose painting using OE-MRI, and to optimise the technique for real-time biology guided adaptive radiotherapy that has short scan time, rapid analysis and sufficient QA procedures, to be performed while the patient lies in the scanner.

Conflicts of interest

G.J.M. Parker is an employee of and holds ownership interest (including patents) in Bioxydyn Limited.

Declaration of Competing Interest

The authors declare that they have no known competing financial interests or personal relationships that could have appeared to influence the work reported in this paper.

Acknowledgements

Appendix A. Supplementary material

Supplementary data to this article can be found online at https://doi.org/10.1016/j.radonc.2023.109592.

References

[1] Wilson WR, Hay MP. Targeting hypoxia in cancer therapy. Nat Rev Cancer 2011;11:393–410.
[2] Nordsmark M, Bentzen SM, Rudat V, Brizel D, Lartigau E, Stadler P, et al. Prognostic value of tumor oxygenation in 397 head and neck tumors after primary radiation therapy. an international multi-center study. Radiother Oncol 2005;77:18–24.
[3] Zips D, Zöphel K, Abolmaali N, Perrin R, Abramyuk A, Haase R, et al. Exploratory prospective trial of hypoxia-specific PET imaging during radiochemotherapy in patients with locally advanced head-and-neck cancer. Radiother Oncol 2012;105:21–8.
[4] Gray LH, Conger AD, Ebert M, Hornsey S, Scott OC. The concentration of oxygen dissolved in tissues at the time of irradiation as a factor in radiotherapy. Br J Radiol 1953;26:638–48.
[5] Sørensen BS, Horsman MR. Tumor hypoxia: impact on radiation therapy and molecular pathways. Front Oncol 2020;10:562.
[6] Toustrup K, Sørensen BS, Lassen P, Wiuf C, Alsner J, Overgaard J, et al. Gene expression classifier predicts for hypoxic modification of radiotherapy with nimorazole in squamous cell carcinomas of the head and neck. Radiother Oncol 2012;102:122–9.
[7] Overgaard J. Hypoxic modification of radiotherapy in squamous cell carcinoma of the head and neck–a systematic review and meta-analysis. Radiother Oncol 2011;100:22–32.
[8] Taylor CT, Colgan SP. Regulation of immunity and inflammation by hypoxia in immunological niches. Nat Rev Immunol 2017;17:774–85.
[9] Thorwarth D. Biologically adapted radiation therapy. Z Med Phys 2018;28:177–83.
[10] Horsman MR, Mortensen LS, Petersen JB, Busk M, Overgaard J. Imaging hypoxia to improve radiotherapy outcome. Nat Rev Clin Oncol 2012;9:674–87.
[11] Buffa FM, Harris AL, West CM, Miller CJ. Large meta-analysis of multiple cancers reveals a common, compact and highly prognostic hypoxia metagene. Br J Cancer 2010;102:428–35.
[12] Thiruthaneeswaran N, Bibby BAS, Yang L, Hoskin PJ, Bristow RG, Choudhury A, et al. Lost in application: measuring hypoxia for radiotherapy optimisation. Eur J Cancer 2021;148:260–76.
[13] Hammond E, Asselin M-C, Forster D, O'Connor JP, Senra J, Williams K. The meaning, measurement and modification of hypoxia in the laboratory and the clinic. Clin Oncol 2014;26:277–88.
[14] Fleming IN, Manavaki R, Blower PJ, West C, Williams KJ, Harris AL, et al. Imaging tumour hypoxia with positron emission tomography. Br J Cancer 2015;112:238–50.
[15] Dewhirst MW, Birer SR. Oxygen-enhanced MRI is a major advance in tumor hypoxia imaging. Cancer Res 2016;76:769–72.
[16] O'Connor JP, Jackson A, Buonaccorsi GA, Buckley DL, Roberts C, Watson Y, et al. Organ-specific effects of oxygen and carbogen gas inhalation on tissue longitudinal relaxation times. Magn Reson Med 2007;58:490–6.
[17] O'Connor JP, Boult JK, Jamin Y, Babur M, Finegan KG, Williams KJ, et al. Oxygen-enhanced MRI accurately identifies, quantifies, and maps tumor hypoxia in preclinical cancer models. Cancer Res 2016;76:787–95.
[18] Salem A, Little RA, Latif A, Featherstone AK, Babur M, Peset I, et al. Oxygen-enhanced MRI is feasible, repeatable, and detects radiotherapy-induced change in hypoxia in xenograft models and in patients with non-small cell lung cancer. Clin Cancer Res 2019;25:3818–29.
[19] Hallac RR, Zhou H, Pidikiti R, Song K, Stojadinovic S, Zhao D, et al. Correlations of noninvasive BOLD and TOLD MRI with pO2 and relevance to tumor radiation response. Magn Reson Med 2014;71:1863–73.
[20] O'Connor JPB, Robinson SP, Waterton JC. Imaging tumour hypoxia with oxygen-enhanced MRI and BOLD MRI. Br J Radiol 2019;92:20180642.
[21] Tijssen RHN, Philippens MEP, Paulson ES, Glitzner M, Chugh B, Wetscherek A, et al. MRI commissioning of 1.5T MR-linac systems - a multi-institutional study. Radiother Oncol 2019;132:114–20.
[22] Datta A, Aznar MC, Dubec M, Parker GJM, O'Connor JPB. Delivering Functional Imaging on the MRI-Linac: current Challenges and Potential Solutions. Clin Oncol (R Coll Radiol) 2018;30:702–10.
[23] van Houdt PJ, Yang Y, van der Heide UA. Quantitative magnetic resonance imaging for biological image-guided adaptive radiotherapy. Front Oncol 2020;10:615643.
[24] Klein S, Staring M, Murphy K, Viergever MA, Pluim JP. elastix: a toolbox for intensity-based medical image registration. IEEE Trans Med Imaging 2010;29:196–205.
[25] Huen I, Morris DM, Wright C, Parker GJ, Sibley CP, Johnstone ED, et al. R1 and R2 * changes in the human placenta in response to maternal oxygen challenge. Magn Reson Med 2013;70:1427–33.
[26] Bland JM, Altman DG. Measurement error. BMJ 1996;313:744.
[27] Obuchowski NA, Reeves AP, Huang EP, Wang XF, Buckler AJ, Kim HJ, et al. Quantitative imaging biomarkers: a review of statistical methods for computer algorithm comparisons. Stat Methods Med Res 2015;24:68–106.
[28] Barnhart HX, Barboriak DP. Applications of the repeatability of quantitative imaging biomarkers: a review of statistical analysis of repeat data sets. Transl Oncol 2009;2:231–5.
[29] Raunig DL, McShane LM, Pennello G, Gatsonis C, Carson PL, Voyvodic JT, et al. Quantitative imaging biomarkers: a review of statistical methods for technical performance assessment. Stat Methods Med Res 2015;24:27–67.
[30] Kooreman ES, van Houdt PJ, Keesman R, Pos FJ, van Pelt VWJ, Nowee ME, et al. ADC measurements on the Unity MR-linac - a recommendation on behalf of the Elekta Unity MR-linac consortium. Radiother Oncol 2020;153:106–13.
[31] Kooreman ES, van Houdt PJ, Keesman R, van Pelt VWJ, Nowee ME, Pos F, et al. Daily Intravoxel Incoherent Motion (IVIM) in prostate cancer patients during MR-guided radiotherapy-a multicenter study. Front Oncol 2021;11:705964.
[32] Akdag O, Mandija S, van Lier ALHM, Borman PTS, Schakel T, Alberts E, et al. Feasibility of cardiac-synchronized quantitative T. Phys Imaging Radiat Oncol 2022;21:153–9.
[33] Chan RW, Lawrence LSP, Oglesby RT, Chen H, Stewart J, Theriault A, et al. Chemical exchange saturation transfer MRI in central nervous system tumours on a 1.5 T MR-Linac. Radiother Oncol 2021;162:140–9.
[34] Tadamura E, Hatabu H, Li W, Prasad PV, Edelman RR. Effect of oxygen inhalation on relaxation times in various tissues. J Magn Reson Imaging 1997;7:220–5.
[35] Winter JD, Akens MK, Cheng HL. Quantitative MRI assessment of VX2 tumour oxygenation changes in response to hyperoxia and hypercapnia. Phys Med Biol 2011;56:1225–42.
[36] O'Connor JP, Naish JH, Parker GJ, Waterton JC, Watson Y, Jayson GC, et al. Preliminary study of oxygen-enhanced longitudinal relaxation in MRI: a potential novel biomarker of oxygenation changes in solid tumors. Int J Radiat Oncol Biol Phys 2009;75:1209–15.
[37] Little RA, Jamin Y, Boult JKR, Naish JH, Watson Y, Cheung S, et al. Mapping hypoxia in renal carcinoma with oxygen-enhanced MRI: comparison with intrinsic susceptibility MRI and pathology. Radiology 2018;288:739–47.
[38] Linnik IV, Scott ML, Holliday KF, Woodhouse N, Waterton JC, O'Connor JP, et al. Noninvasive tumor hypoxia measurement using magnetic resonance imaging in murine U87 glioma xenografts and in patients with glioblastoma. Magn Reson Med 2014;71:1854–62.
[39] Bluemke E, Bulte D, Bertrand A, George B, Cooke R, Chu KY, et al. Oxygen-enhanced MRI MOLLI T1 mapping during chemoradiotherapy in anal squamous cell carcinoma. Clin Transl Radiat Oncol 2020;22:44–9.
[40] Bane O, Besa C, Wagner M, Oesingmann N, Zhu H, Fiel MI, et al. Feasibility and reproducibility of BOLD and TOLD measurements in the liver with oxygen and carbogen gas challenge in healthy volunteers and patients with hepatocellular carcinoma. J Magn Reson Imaging 2016;43:866–76.
[41] O'Connor JP, Jackson A, Parker GJ, Roberts C, Jayson GC. Dynamic contrast-enhanced MRI in clinical trials of antivascular therapies. Nat Rev Clin Oncol 2012;9:167–77.
[42] O'Connor JP, Aboagye EO, Adams JE, Aerts HJ, Barrington SF, Beer AJ, et al. Imaging biomarker roadmap for cancer studies. Nat Rev Clin Oncol 2017;14:169–86.
[43] Sullivan DC, Obuchowski NA, Kessler LG, Raunig DL, Gatsonis C, Huang EP, et al. Metrology Standards for Quantitative Imaging Biomarkers. Radiology 2015;277:813–25.